Letter

Ultrathin Pyroelectric Photodetector with Integrated Polarization-Sensing Metasurface

Nathaniel C. Wilson, Eunso Shin, Rachel E. Bangle, Stefan B. Nikodemski, Jarrett H. Vella, and Maiken H. Mikkelsen*

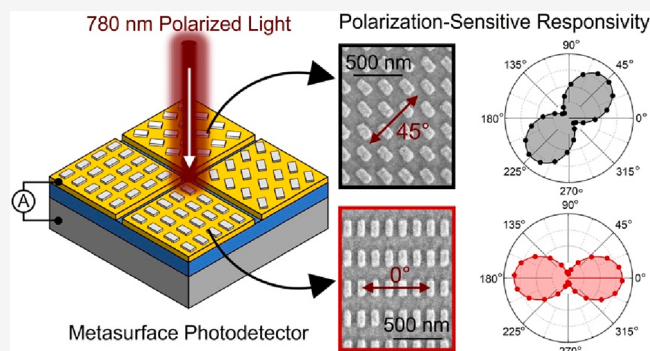Cite This: Nano Lett. 2023, 23, 8547−8552

Read Online

ACCESS | Metrics & More | Article Recommendations | Supporting Information

ABSTRACT: An abundance of metallic metasurfaces have been realized with miniscule, intricate features capable of tailored scattering, reflection, and absorption; however, high losses through heat limit their use in optoelectronics. Here, codesign of a detector and a polarization-sensing metasurface overcomes this challenge by utilizing the heat generation for integrated pyroelectric detection of the incoming light polarization. Using a nanogap metasurface with asymmetric metallic elements, polarization-sensitive photodetection exhibits high extinction ratios up to 19 for orthogonally polarized light and allows extraction of Stokes parameters with <12% deviation from theoretical values. This polarization-sensitive photodetector is ultrathin, consisting of active layers of only 290 nm, and exhibits fast response times of ~2 ns. The structure is fully integrated, requiring no external cameras, detectors, or power sources, and points toward the creation of layered, multifunctional devices that utilize exotic metasurface properties for novel and compact sensing and imaging.

KEYWORDS: polarization sensing, photodetection, metasurfaces, pyroelectrics

Properties of light, beyond those captured in traditional imaging, carry valuable information about the object with which the light has interacted. In particular, the polarization state of light reveals information about *e.g.* the object's shape, texture, orientation, or strain.[1,2] As such, polarimetry represents an invaluable tool across a wide range of fields including astronomy, agriculture, environmental monitoring, and medicine.[3−5] Although a variety of schemes for polarization sensing and imaging exist, most require light to be split between multiple cameras, each with sets of bulky optics which control or modulate the light's polarization.[1,6,7] Recent advances in metasurfaces, however, have developed the capability to sense and control light's polarization with subwavelength optical elements[8] through polarization-selective absorption, transmission, reflection, and beam steering.[9−12] Examples include metasurfaces that can detect linear[13,14] and circular[15−17] light polarization, quantify the full Stokes parameters,[18−27] or exhibit more exotic functionalities such as orbital angular momentum sensing[28] or waveplate behavior.[29] Despite utilizing ultrathin metasurfaces, all these examples outcouple light from the metasurfaces to external cameras or photodiodes, resulting in bulky systems. Recently, a few examples of on-chip metasurface-enabled polarimeters have been reported that allow for more integrated devices;[30−34] however, they either require outside power in the form of an applied bias[30,32,34,35] or suffer from low

extinction ratios between polarization states in the visible/near-infrared region.[30−32,35] As such, a fully integrated, ultrathin polarization-sensitive photodetector that has a high extinction ratio and requires no external cameras, optics, or power is highly desirable.

Here, we utilize well-established metasurface structures to codesign a metasurface and pyroelectric photodetector to realize an integrated polarization-sensitive photodetector that is ultrathin, with active layers of only 290 nm total; exhibits large extinction ratios up to 19; and does not require external cameras, optics, or power sources. Moreover, the integrated thermal detectors display high-speed response times, with a 10−90% rise time of 2 ns, resulting from the ultrathin device structure. The photodetector consists of an array of silver rectangles (75 × 150 nm) separated from a gold film by a 10 nm dielectric layer, also termed a nanogap metasurface, with an underlying 165 nm AlN pyroelectric thermal detection layer. The codesign of the metasurface and pyroelectric structure herein allows the conversion of absorbed light to heat in the
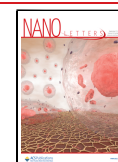
metallic metasurface, which is often a loss pathway in optoelectronic applications, to act as the operative signal. The metasurface acts as an antenna by efficiently absorbing light at its resonant wavelength (Figure 1a), and the absorbed
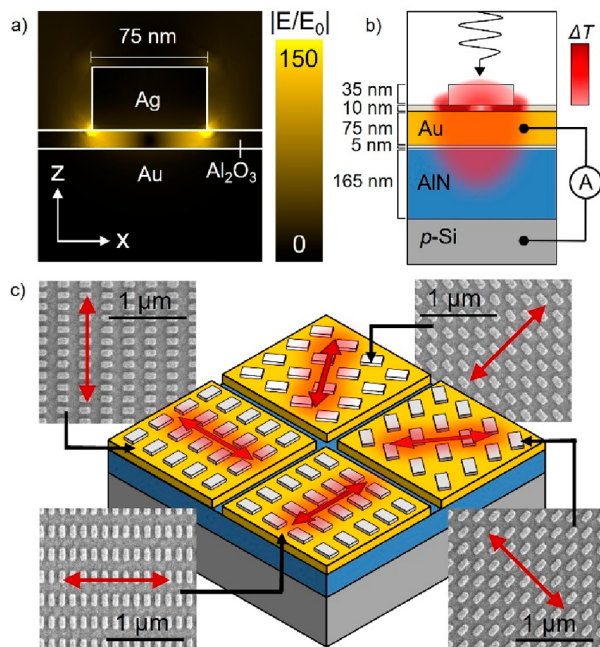

Figure 1. (a) COMSOL simulation of nanogap cavity (side view) upon illumination with resonant 740 nm light. Antenna-like light absorption generates intense electric fields in the gap region. (b) Schematic representation of heat generation (ΔT, side view) within the nanogap cavity. Light energy is converted to heat, which diffuses to the pyroelectric AlN layer on picosecond time scales. This leads to a measurable device current response. (c) Schematic representation of four photodetectors optimized for absorption of light polarized at the angle of the red arrows. Detectors and nanoparticles are not drawn to scale. Inset: SEM images associated with each photodetector show rectangular nanoparticles of ∼75 nm × 150 nm at different orientations.

light is converted to heat through collisions between the oscillating plasmonic electrons and lattice atoms (Figure 1b).[36,37] Previous simulations have demonstrated that heat is generated and propagates downward through the metal film on picosecond time scales.[38] The generated heat is exploited by the underlying pyroelectric AlN photodetector, which is spontaneously polarized at room temperature and experiences a change in polarization in response to a temperature change.[38−40] This generates a measurable current according to

$$I_p(t) = Ap\frac{dT}{dt} \tag{1}$$

where A is the illuminated area of the device, p is the pyroelectricity coefficient of AlN, and dT/dt is the AlN temperature change with respect to time (details in SI). Light polarization sensitivity arises from the designed asymmetry in the metasurface, as light is most effectively absorbed when its angle of linear polarization (AoLP) aligns with the resonant axis of the rectangular nanoparticles. As such, four devices with rectangular nanoparticles rotated in 45° steps, as seen in Figure 1c, are used to explicitly determine the AoLP and Stokes parameters for arbitrarily polarized incident light.

White light reflectance spectra illustrate the spectrally selective near-perfect absorbance of the metasurface. Reflectance exhibits a stark (∼75%) decrease centered at the plasmon resonance at 740 nm (Figure 2a, Figure S4) resulting
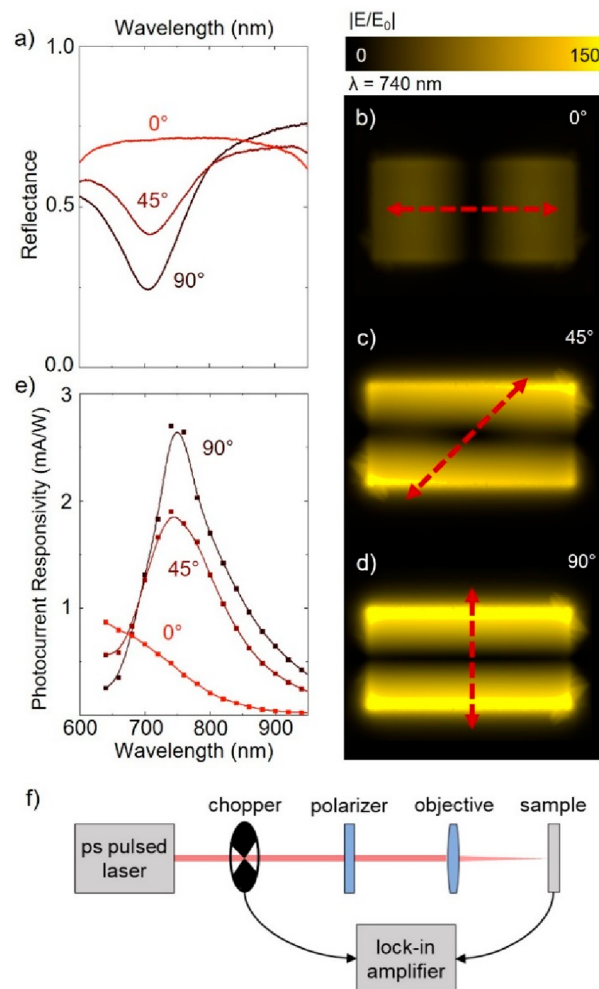

Figure 2. (a) White light reflectance spectra for incident angle of linear polarizations of 0°, 45°, and 90°, where 0° is defined as being aligned with the rectangular nanoparticle long axis. (b−d) COMSOL finite element simulations of the nanogap cavity (x−y plane, 1 nm below silver rectangle) upon illumination with 740 nm light with the indicated angle of linear polarization relative to the nanoparticle short axis. Arrows illustrate the polarization angle. (e) Photocurrent responsivity as a function of excitation wavelength upon illumination with a laser chopped at a frequency of 3.9 kHz at the indicated angle of linear polarization. (f) Simplified schematic of experimental setup for photocurrent responsivity measurements.

from efficient absorption at this wavelength. Finite element simulations show that this corresponds to the absorption of a gap plasmon mode, which propagates along the short axis of the rectangular nanoparticle (Figure 2b). Because light is most efficiently coupled into the gap plasmon mode when the incident angle of linear polarization aligns with the nanoparticle axis, the absorbance peak exhibits polarization anisotropy. Absorbance is maximized for AoLP = 90° for the nanoparticle orientation shown in Figure 2, while rotation of the AoLP by 90° nearly completely suppresses absorption (Figure 2a). These observations are in agreement with finite element simulations (Figure 2b−d), which exhibit distinct,
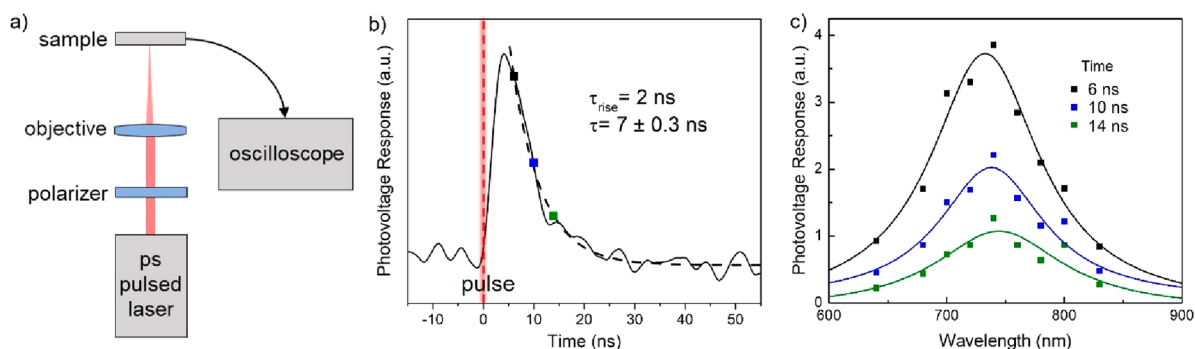
Figure 3. (a) Simplified schematic of experimental setup for time-resolved photovoltage measurements. (b) Time-resolved photovoltage upon 10 MHz pulsed, 740 nm excitation with AoLP = 0°. A single exponential fit (dashed line) shows a 10−90% rise time of 2 ns and a decay time of 7 ns. Colored points correspond to the time points of photovoltage spectra shown in (c). (c) Photovoltage spectra taken at the indicated time delay after excitation at time zero. Solid lines are guides to the eye.

polarization-dependent gap plasmon modes corresponding to both the long and short axes.[12] The resonant wavelength of each mode is determined by the respective side length (Figure S4). Specifically for these absorbers, the rectangle short axis exhibits an absorption mode with an ∼740 nm resonance, while the long axis exhibits a mode >1 μm, beyond the measured device responsivity range. This allows the isolation of polarization-sensitive near-infrared absorption within the devices.

The photocurrent responsivity of the devices upon excitation with chopped linearly polarized light in the experimental scheme shown in Figure 2f follows both the spectral response and the polarization anisotropy of the metasurface absorption. As the wavelength of the incident light is tuned, the photocurrent responsivity of the devices measured with a lock-in amplifier follows the spectral shape of the gap plasmon absorption (Figure 2e, Figure S5). This illustrates the role of the metasurface as light absorber and photothermal converter, as control devices with no rectangular nanoparticles display a photocurrent which follows the spectral shape of a gold film and which is 3 orders of magnitude smaller than that of metasurface-functionalized devices (Figure S6). Further, as the AoLP of the incident light is tuned by rotation of a linear polarizer, device photocurrent responsivity follows the polarization anisotropy of the metasurface absorption. The photocurrent increases linearly with chopper frequency (Figure S7), which is characteristic of a pyroelectric response when the modulation is much slower than the device time constant.[41] This suggests heating of the AlN to indeed be the operative mechanism of photocurrent generation, in agreement with previous studies.[38]

The structure displays simultaneous spectral selectivity and polarization sensing, as determined by the size and orientation of the rectangular nanoparticles. Photocurrent responsivity is maximized when the AoLP aligns with the short axis of the rectangular nanoparticles and is efficiently suppressed when the AoLP is rotated by 90°, with a responsivity ratio of the "on" and "off" states as high as 19:1. Noise equivalent power for the devices at the responsivity peak is calculated to be 16−24 pW/$\sqrt{Hz}$, which is similar to commercially available detectors (Figure S8).

The time-resolved spectral photovoltage response shows that these photodetectors operate on an RC-limited, nanosecond time scale. Upon illumination with picosecond pulsed laser light at the wavelength of the responsivity peak as shown in Figure 3a, the devices produce a time-resolved photo-

response which exhibits a 10−90% rise time of ∼2 ns and a decay time constant of ∼7 ns (Figure 3b). The polarization of the laser is aligned with the nanoparticle short axis to maximize the photovoltage response. The theoretical RC time constant assuming ideal geometry and material values is 5.09 ns, meaning that the device speeds observed here approach the RC limit (details in SI). Both rise and fall times are independent of the excitation wavelength within experimental error. Further, the amplitude of the time-resolved photovoltage response at a series of time points exhibits a spectral peak in good agreement with the metasurface absorption (Figure 3c). This indicates that the time-resolved photovoltages measured at high frequency indeed result from heating induced by gap-plasmon absorption. Based on the measured rise time, these devices show fast response times with a −3 dB bandwidth of ∼175 MHz. Further, the RC limited response suggests that device speeds could be enhanced by reducing the active area to decrease the device capacitance and, thus, the RC time constant.

To explicitly determine the angle of linear polarization for any incident light, four detectors are fabricated with silver nanoparticles rotated in 45° steps (Figure 4a−d). For each device, metasurface absorption is maximized when the incident light AoLP aligns with the short axis of the nanoparticle and is suppressed for light with a 90° relative polarization rotation (Figure 4e−h, Figure S5). Device responsivities as a function of incident wavelength correlate closely with the measured reflectance spectra (Figure S4). In Figure 4e−h, absorption and photocurrent responsivity values are quantified at a single wavelength for which the extinction ratio of the on-axis and orthogonal excitations is maximized. For each device, both the responsivity and absorption exhibit sinusoidal dependence on the incident AoLP with up to 94.7% responsivity suppression between the "on" and "off" states (Figure 4e−h).

The relative outputs of the four individual photodetectors allow explicit determination of the angle of linear polarization of any arbitrary incident polarized light, which would not be possible with a single detector (Figure 5a). Devices show photocurrent ratios of 15−19 for incident light with orthogonal AoLP, which results in at most 12% deviation from an ideal device response. This high contrast of "on" and "off" states allows calculation of Stokes parameters, vector values S_0, S_1, S_2, and S_3 which uniquely describe all possible polarization states of light. The value S_0 serves to normalize the photocurrent outputs, and the value S_3, which describes circular polarization, is 0 for the linearly polarized light
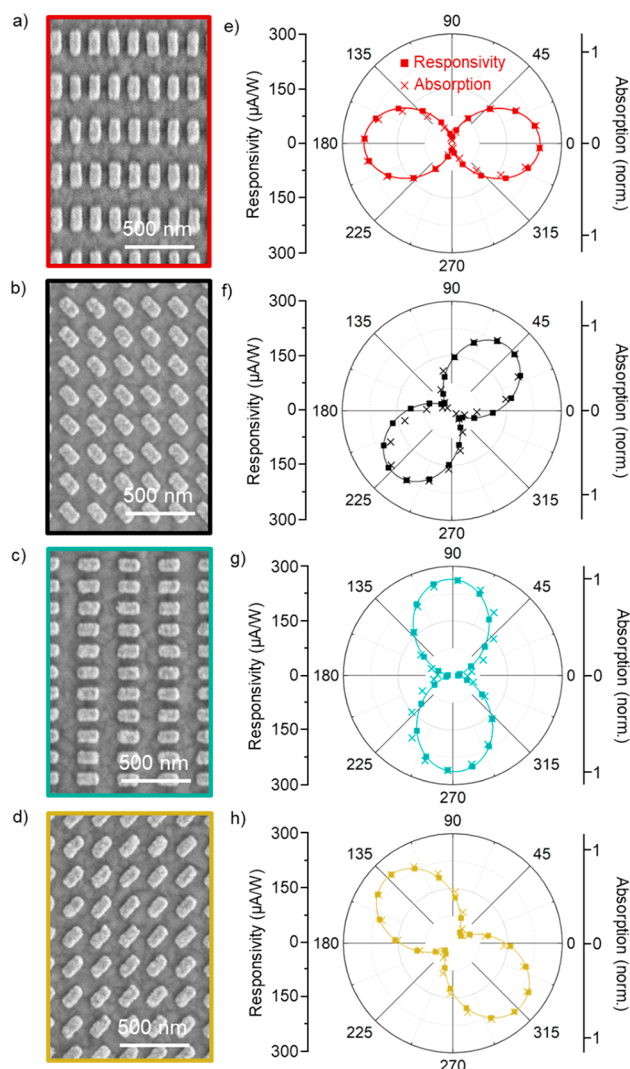
Figure 4. (a−d) Scanning electron microscopy (SEM) images of metasurfaces composed of silver rectangles corresponding to each detector. (e−h) Polar absorption (crosses) and responsivity (squares) measured at a single wavelength at which the orthogonal extinction ratio is maximized for each device. Solid lines represent fits of the sinusoidal form (Equation S3).

Figure 5. (a) Relative photoresponse from four detectors with nanoparticle orientation rotated in 45° steps for incident light with AoLP = 0°, 45°, 90°, 135°. (b) Calculated Stokes parameters normalized to S_0 for incident light with 0°−360° AoLP plotted on a Poincaré sphere.

employed herein. As such, S_1 and S_2 values completely describe the AoLP of the incident light (Figure 5b, details in SI). Experimental values show good agreement with theoretical values calculated for ideal detectors, demonstrating the ability for accurate polarization determination using the fabricated structures.

The fabricated photodetectors display a combination of high-sensitivity, high-speed, and high-accuracy polarization sensing in a fully integrated and ultrathin 290 nm structure. In particular, the experimentally realized devices exhibit 19:1 polarization selectivity and <12% deviation from expected Stokes parameters with RC-limited response times and 16−24 pW/$\sqrt{\text{Hz}}$ noise equivalent power. These features result from codesign of the metasurface and the photodetection mechanism in which pairing a metallic metasurface with a pyroelectric film allows the metasurface to serve the dual roles of a polarization-sensitive, wavelength-selective optical absorber and a photothermal converter. This simultaneous polarization filtering and detection leads to a device which
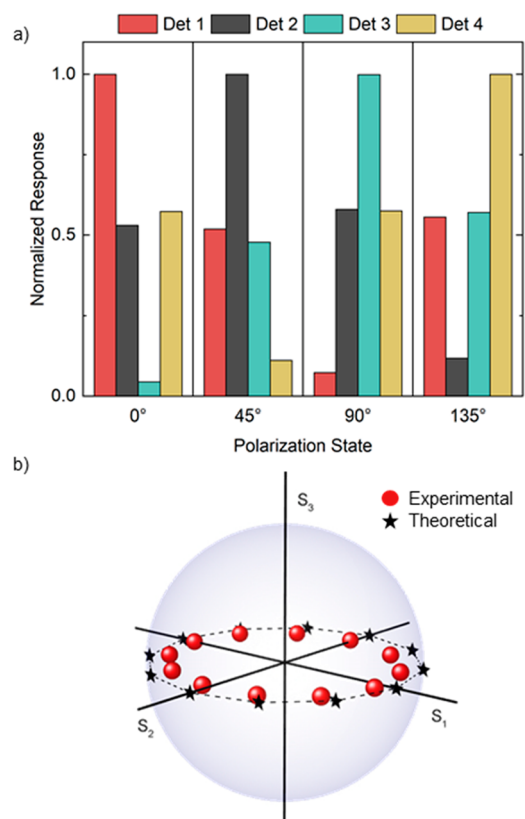
requires no external cameras, power sources, or bulky optics. Further, the small mode volumes of the metasurface and the thinness of the pyroelectric film result in active layers only 290 nm thick. Much of this thickness is the AlN pyroelectric film (165 nm), which may be thinned even further.[42] Recent reports have shown substantial enhancement of pyroelectric coefficients in some extremely thin films suggesting that sub-100 nm thick devices might be possible.[43] The thinness of these photodetectors also presents an exciting opportunity to combine multiple metasurfaces to create layered, multifunctional devices, leveraging the vast library of exotic metasurfaces realized in recent years to control and sense light fields. Additional layers with actively controlled refractive indices, such as optofluidic channels, liquid crystals, or electrochromic materials, could also allow wavelength tunability or active polarization switching.[44−46] This has the potential to enable ultracompact and novel on-chip photodetection and imaging devices.

■ ASSOCIATED CONTENT

ⓢ Supporting Information

The Supporting Information is available free of charge at https://pubs.acs.org/doi/10.1021/acs.nanolett.3c02341.

> Device fabrication details, AlN material characterization, measurement details, additional absorption and responsivity spectra, frequency-dependent responsivity, noise equivalent power spectra, electric field simulations, and discussion of Stokes parameters (PDF)

■ AUTHOR INFORMATION

Corresponding Author

    Maiken H. Mikkelsen − *Department of Electrical and Computer Engineering, Duke University, Durham, North Carolina 27708, United States;* ⊙ orcid.org/0000-0002-0487-7585; Email: m.mikkelsen@duke.edu

Authors

    Nathaniel C. Wilson − *Department of Physics, Duke University, Durham, North Carolina 27708, United States*

    Eunso Shin − *Department of Electrical and Computer Engineering, Duke University, Durham, North Carolina 27708, United States*

    Rachel E. Bangle − *Department of Electrical and Computer Engineering, Duke University, Durham, North Carolina 27708, United States*

    Stefan B. Nikodemski − *KBR, Beavercreek, Ohio 45431, United States*

    Jarrett H. Vella − *Sensors Directorate, Air Force Research Laboratory, Wright−Patterson Air Force Base, Dayton, Ohio 45433, United States*

Complete contact information is available at:
https://pubs.acs.org/10.1021/acs.nanolett.3c02341

Notes

The authors declare no competing financial interest.

■ REFERENCES

(1) Tyo, J. S.; Goldstein, D. L.; Chenault, D. B.; Shaw, J. A. Review of Passive Imaging Polarimetry for Remote Sensing Applications. *Appl. Opt.* **2006**, *45* (22), 5453−5469.

(2) Walraven, R. Polarization Imagery. *Opt. Eng.* **1981**, *20* (1), 14−18.

(3) Hough, J. Polarimetry: A Powerful Diagnostic Tool in Astronomy. *Astron. Geophys.* **2006**, *47* (3), 3.31−3.35.

(4) Ignatenko, D. N.; Shkirin, A. V.; Lobachevsky, Y. P.; Gudkov, S. V. Applications of Mueller Matrix Polarimetry to Biological and Agricultural Diagnostics: A Review. *Appl. Sci.* **2022**, *12* (10), 5258.

(5) He, C.; He, H.; Chang, J.; Chen, B.; Ma, H.; Booth, M. J. Polarisation Optics for Biomedical and Clinical Applications: A Review. *Light Sci. Appl.* **2021**, *10* (1), 194.

(6) Dong, J.; Zhou, H. Polarimeters from Bulky Optics to Integrated Optics: A Review. *Opt. Commun.* **2020**, *465*, 125598.

(7) Singh, K.; Tabebordbar, N.; Forbes, A.; Dudley, A. Digital Stokes Polarimetry and Its Application to Structured Light: Tutorial. *JOSA A* **2020**, *37* (11), C33−C44.

(8) Shi, Z.; Capasso, F.; Rubin, N. A. Polarization in Diffractive Optics and Metasurfaces. *Adv. Opt. Photonics* **2021**, *13* (4), 836−970.

(9) Gansel, J. K.; Thiel, M.; Rill, M. S.; Decker, M.; Bade, K.; Saile, V.; von Freymann, G.; Linden, S.; Wegener, M. Gold Helix Photonic Metamaterial as Broadband Circular Polarizer. *Science.* **2009**, *325* (5947), 1513−1515.

(10) Zhao, Y.; Belkin, M. A.; Alù, A. Twisted Optical Metamaterials for Planarized Ultrathin Broadband Circular Polarizers. *Nat. Commun.* **2012**, *3* (1), 1−7.

(11) Zhu, A. Y.; Chen, W. T.; Zaidi, A.; Huang, Y. W.; Khorasaninejad, M.; Sanjeev, V.; Qiu, C. W.; Capasso, F. Giant Intrinsic Chiro-Optical Activity in Planar Dielectric Nanostructures. *Light Sci. Appl.* **2018**, *7* (2), 17158−17158.

(12) Shen, Q.; Boyce, A. M.; Yang, G.; Mikkelsen, M. H. Polarization-Controlled Nanogap Cavity with Dual-Band and Spatially Overlapped Resonances. *ACS Photonics* **2019**, *6* (8), 1916−1921.

(13) Pelzman, C.; Cho, S. Y. Multispectral and Polarimetric Photodetection Using a Plasmonic Metasurface. *J. Appl. Phys.* **2018**, *123* (4), 043107.

(14) Pors, A.; Bozhevolnyi, S. I. Plasmonic Metasurfaces for Efficient Phase Control in Reflection. *Opt. Express* **2013**, *21* (22), 27438−27451.

(15) Khorasaninejad, M.; Crozier, K. B. Silicon Nanofin Grating as a Miniature Chirality-Distinguishing Beam-Splitter. *Nat. Commun.* **2014**, *5* (1), 1−6.

(16) Kildishev, A.; Shalaev, V.; Shaltout, A.; Liu, J. Photonic Spin Hall Effect in Gap-Plasmon Metasurfaces for on-Chip Chiroptical Spectroscopy. *Optica* **2015**, *2* (10), 860−863.

(17) Khorasaninejad, M.; Chen, W. T.; Zhu, A. Y.; Oh, J.; Devlin, R. C.; Rousso, D.; Capasso, F. Multispectral Chiral Imaging with a Metalens. *Nano Lett.* **2016**, *16* (7), 4595−4600.

(18) Arbabi, E.; Kamali, S. M.; Arbabi, A.; Faraon, A. Full-Stokes Imaging Polarimetry Using Dielectric Metasurfaces. *ACS Photonics* **2018**, *5* (8), 3132−3140.

(19) Ding, F.; Pors, A.; Chen, Y.; Zenin, V. A.; Bozhevolnyi, S. I. Beam-Size-Invariant Spectropolarimeters Using Gap-Plasmon Metasurfaces. *ACS Photonics* **2017**, *4* (4), 943−949.

(20) Basiri, A.; Chen, X.; Bai, J.; Amrollahi, P.; Carpenter, J.; Holman, Z.; Wang, C.; Yao, Y. Nature-Inspired Chiral Metasurfaces for Circular Polarization Detection and Full-Stokes Polarimetric Measurements. *Light Sci. Appl.* **2019**, *8* (1), 1−11.

(21) Rubin, N. A.; D'Aversa, G.; Chevalier, P.; Shi, Z.; Chen, W. T.; Capasso, F. Matrix Fourier Optics Enables a Compact Full-Stokes Polarization Camera. *Science.* **2019**, *365* (6448), eaax1839.

(22) Yang, Z.; Wang, Z.; Wang, Y.; Feng, X.; Zhao, M.; Wan, Z.; Zhu, L.; Liu, J.; Huang, Y.; Xia, J.; Wegener, M. Generalized Hartmann-Shack Array of Dielectric Metalens Sub-Arrays for Polarimetric Beam Profiling. *Nat. Commun.* **2018**, *9* (1), 1−7.

(23) Lee, K.; Yun, H.; Mun, S. E.; Lee, G. Y.; Sung, J.; Lee, B. Ultracompact Broadband Plasmonic Polarimeter. *Laser Photon. Rev.* **2018**, *12* (3), 1700297.

(24) Chen, W. T.; Török, P.; Foreman, M. R.; Liao, C. Y.; Tsai, W. Y.; Wu, P. R.; Tsai, D. P. Integrated Plasmonic Metasurfaces for Spectropolarimetry. *Nanotechnology* **2016**, *27* (22), 224002.

(25) Pors, A.; Nielsen, M. G.; Bozhevolnyi, S. I. Plasmonic Metagratings for Simultaneous Determination of Stokes Parameters. *Optica* **2015**, *2* (8), 716−723.

(26) Yue, W.; Tian, C.; Yang, S.; Plum, E.; Xu, Q.; Zhang, S.; Zhang, X.; Zhang, X.; Han, J.; Zhang, W. Direct Polarization Measurement Using a Multiplexed Pancharatnam-Berry Metahologram. *Optica* **2019**, *6* (9), 1190−1198.

(27) Balthasar Mueller, J. P.; Leosson, K.; Capasso, F. Ultracompact Metasurface In-Line Polarimeter. *Optica* **2016**, *3* (1), 42−47.

(28) Maguid, E.; Yulevich, I.; Yannai, M.; Kleiner, V.; Brongersma, M. L.; Hasman, E. Multifunctional Interleaved Geometric-Phase Dielectric Metasurfaces. *Light Sci. Appl.* **2017**, *6* (8), No. e17027.

(29) Zhao, Y.; Alu, A. Manipulating Light Polarization with Ultrathin Plasmonic Metasurfaces. *Phys. Rev. B* **2011**, *84* (20), 205428.

(30) Li, W.; Coppens, Z. J.; Besteiro, L. V.; Wang, W.; Govorov, A. O.; Valentine, J. Circularly Polarized Light Detection with Hot Electrons in Chiral Plasmonic Metamaterials. *Nat. Commun.* **2015**, *6* (1), 1−7.

(31) Hong, J.; van de Groep, J.; Lee, N.; Kim, S. J.; Lalanne, P.; Kik, P. G.; Brongersma, M. L. Nonlocal Metasurface for Circularly Polarized Light Detection. *Optica* **2023**, *10* (1), 134−141.

(32) Panchenko, E.; Cadusch, J. J.; James, T. D.; Roberts, A. Plasmonic Metasurface-Enabled Differential Photodetectors for Broadband Optical Polarization Characterization. *ACS Photonics* **2016**, *3* (10), 1833−1839.

(33) Strømme, M.; Ahuja, R.; Niklasson, G. A. New Probe of the Electronic Structure of Amorphous Materials. *Phys. Rev. Lett.* **2004**, *93* (20), 206403.

(34) Li, L.; Wang, J.; Kang, L.; Liu, W.; Yu, L.; Zheng, B.; Brongersma, M. L.; Werner, D. H.; Lan, S.; Shi, Y.; Xu, Y.; Wang, X. Monolithic Full-Stokes Near-Infrared Polarimetry with Chiral Plasmonic Metasurface Integrated Graphene-Silicon Photodetector. *ACS Nano* **2020**, *14* (12), 16634−16642.

(35) Li, C.-Y.; Chen, C.; Liu, Y.; Su, J.; Qi, D.-X.; He, J.; Fan, R.-H.; Cai, Q.; Li, Q.; Peng, R.; Huang, X.-R.; Wang, M. Multiple-Polarization-Sensitive Photodetector Based on a Perovskite Metasurface. *Opt. Lett.* **2022**, *47* (3), 565−568.

(36) Govorov, A. O.; Richardson, H. H. Generating Heat with Metal Nanoparticles. *Nano Today* **2007**, *2* (1), 30−38.

(37) Jauffred, L.; Samadi, A.; Klingberg, H.; Bendix, P. M.; Oddershede, L. B. Plasmonic Heating of Nanostructures. *Chem. Rev.* **2019**, *119* (13), 8087−8130.

(38) Stewart, J. W.; Vella, J. H.; Li, W.; Fan, S.; Mikkelsen, M. H. Ultrafast Pyroelectric Photodetection with On-Chip Spectral Filters. *Nat. Mater.* **2020**, *19* (2), 158−162.

(39) Sykes, M. E.; Stewart, J. W.; Akselrod, G. M.; Kong, X.-T. T.; Wang, Z.; Gosztola, D. J.; Martinson, A. B. F. F.; Rosenmann, D.; Mikkelsen, M. H.; Govorov, A. O.; Wiederrecht, G. P. Enhanced Generation and Anisotropic Coulomb Scattering of Hot Electrons in an Ultra-Broadband Plasmonic Nanopatch Metasurface. *Nat. Commun.* **2017**, *8* (1), 986.

(40) Stewart, J. W.; Wilson, N. C.; Mikkelsen, M. H. Nanophotonic Engineering: A New Paradigm for Spectrally Sensitive Thermal Photodetectors. *ACS Photonics* **2021**, *8* (1), 71−84.

(41) Rogalski, A. *Infrared and Terahertz Detectors*, 3rd ed.; CRC Press: 2019; DOI: 10.1201/b21951.

(42) Felmetsger, V. V.; Laptev, P. N.; Graham, R. J. Deposition of Ultrathin AlN Films for High Frequency Electroacoustic Devices. *J. Vac. Sci. Technol. A Vacuum, Surfaces, Film.* **2011**, *29* (2), 021014.

(43) Jiang, J.; Zhang, L.; Ming, C.; Zhou, H.; Bose, P.; Guo, Y.; Hu, Y.; Wang, B.; Chen, Z.; Jia, R.; Pendse, S.; Xiang, Y.; Xia, Y.; Lu, Z.; Wen, X.; Cai, Y.; Sun, C.; Wang, G. C.; Lu, T. M.; Gall, D.; Sun, Y. Y.; Koratkar, N.; Fohtung, E.; Shi, Y.; Shi, J. Giant Pyroelectricity in Nanomembranes. *Nature* **2022**, *607* (7919), 480−485.

(44) Li, Q.; van de Groep, J.; White, A. K.; Song, J.-H.; Longwell, S. A.; Fordyce, P. M.; Quake, S. R.; Kik, P. G.; Brongersma, M. L. Metasurface Optofluidics for Dynamic Control of Light Fields. *Nat. Nanotechnol.* **2022**, *17* (10), 1097−1103.

(45) Sautter, J.; Staude, I.; Decker, M.; Rusak, E.; Neshev, D. N.; Brener, I.; Kivshar, Y. S. Active Tuning of All-Dielectric Metasurfaces. *ACS Nano* **2015**, *9* (4), 4308−4315.

(46) Lee, Y.; Yun, J.; Seo, M.; Kim, S.-J.; Oh, J.; Kang, C. M.; Sun, H.-J.; Chung, T. D.; Lee, B. Full-Color-Tunable Nanophotonic Device Using Electrochromic Tungsten Trioxide Thin Film. *Nano Lett.* **2020**, *20* (8), 6084−6090.